Hindawi
Advances in Civil Engineering
Volume 2021, Article ID 6687124, 11 pages
https://doi.org/10.1155/2021/6687124

Research Article

Large-Scale Model Test of a Micropile Group for Landslide Control

Xueling Liu,[1] Jinkai Yan ,[2] Lei Liu,[3] and Bing Han[4]

[1]*School of Geological Engineering and Geomatics, Chang'an University, Xi'an 710054, China*
[2]*Chinese Academy of Geological Science, Beijing 100037, China*
[3]*Beijing City University, Beijing 100083, China*
[4]*China Institute of Geo-Environmental Monitoring, Beijing 100081, China*

Correspondence should be addressed to Jinkai Yan; yanjinkaisw@163.com

Received 5 March 2021; Revised 27 March 2021; Accepted 7 April 2021; Published 23 April 2021

Academic Editor: Zhixiong Zeng

A large-scale model test on the interaction between a micropile group and a landslide was conducted, to investigate the effect of micropiles on the landsides prevention. The bearing mechanism, force condition, and failure mode of a micropile group for reinforcing landslide were analyzed in detail. The results showed that the thrust force over micropiles induced by landslide showed a trapezoidal distribution, with a higher Earth pressure near the sliding surface. The resistance from the sliding body behind the pile behaved in a parabolically trend. Meanwhile, the resistance force from the sliding bed was distributed unevenly along the height direction, with a higher resistance force near the sliding surface behind the pile. When a landslide occurred, micropiles were subjected to an increase in loading and displacement, eventually to the failure state. The load-bearing sections of the micropiles were all subjected to negative bending moments, with larger bending moments within the half length of pile range near the sliding surface. The maximum negative bending moment occurred at the height of seven times the diameter of the pile above the sliding surface. The damage mode along each row of micropiles was almost the same, showing a damage area within the range of three times the diameter of the pile above and below the sliding surface. The failure of micropile induced by landslides was mainly due to a combination effect of bending and shearing near the sliding surface.

1. Introduction

Micropiles refer to bored piles with the diameter is less than 300 mm, formed by pressure grouting after pores are drilled with strong reinforcement. Due to their convenient and rapid construction, flexible pile placement, and small disturbances to landslides, micropiles are increasingly used in landslide prevention projects [1–10]. Although micropiles have been used to prevent the landsides, the bearing mechanism of micropiles is not fully understood.

Experimental studies have been conducted on the horizontal load-bearing performance of micropiles. For example, through field tests, Zeng et al. [11] preliminarily studied the relationship between the lateral load acting on a single micropile and the required pile length. Richards et al. [12] investigated the lateral load-bearing performance of micropiles. Konagai et al. [13] carried out a detailed analysis on the performance of micropile groups with rigid caps under lateral loading through model tests. However, the micropiles were taken as the pile foundation in the previous studies. The application of micropiles in landslide treatment remains rare and needs to be further studied. Several studies focused on the anti-sliding effect of micropiles via model test. For example, Liang [14] preformed a model test and studied the ultimate flexural bearing capacity test of mini pile featuring steel tube and centered steel bar. Chen [15] presented an investigation into anti-sliding characteristics of high-pressure grouting steel-tube micropiles by model experiments. Zhang [16] carried out model tests to analyze the anti-sliding performance of multiple segmented grouting steel pile group from the aspects of soil pressure and bending of steel pipe. Grouting effect, pile group effect, and failure mode were also discussed. Hu [17] studied the stress deformation characteristics of micropile and the transmission law of a landslide through groups of experiments of different piles spacing under three rows of a micropile reinforcement

debris landslide. Although these researches provided valuable results on this area, the results were basically based on small-scale models. It is necessary to carry out large-scale model tests to study the force and deformation mechanism of micropiles under the action of landslide.

In this study, a large-scale model test regarding the interaction between landslide and micropile groups was conducted. The thrust force on a micropile induced by a landslide was monitored, along with the stress distribution and displacement of micropile. Accordingly, the bearing mechanism, force condition, and failure mode of a micropile group to reinforce a landslide were discussed in detail.

2. Testing Model

2.1. Model Test Design. A model of landslide was generated as a sliding bed and a sliding body above, which consisted of loess as shown in Figure 1. The sliding body was used to trigger the landslide by applying graded loads on the top of the slope. The micropiles were distributed along the slope foot, divided into 5 rows, a total of 23 piles. The top of micropiles was connected with a steel beam. By installing the pressure gauges in front of and behind the micropile, the variations of force on micropiles were monitored. The strain of the pile was tested using the strain gauge attached to the main reinforcement of the micropile. This value was also used to calculate the bending moment of the pile. The deformations of the micropile and the sliding body were recorded by the displacement meter installed at the top of the pile and the toe of landslide. The schematic diagram of the test model is shown in Figure 1.

2.2. Similarity Ratio. According to the test conditions, geometric similarity ratio $C_L = 3$ and elastic modulus similarity ratio $C_E = 1$ were adopted in this study. Based on the principle of similarity theory [10], the similarity ratio of physical quantities was determined as follows: $C_q = 3$, $C_P = 9$, $C_\sigma = 1$, $C_\varepsilon = 1$, $C_{\mathrm{Ac}} = 9$, $C_{\mathrm{As}} = 9$, where C_q denotes the similarity ratio of linear load on the pile body; C_{P} denotes the similarity ratio of concentrated force on the pile body; C_σ denotes the similarity ratio of stress of the pile body; C_ε denotes the similarity ratio of strain of the pile body; C_{Ac} denotes the similarity ratio of cross-sectional area of the pile body; and C_{As} denotes the similarity ratio of cross-sectional area of reinforcement.

2.3. Materials

2.3.1. Sliding Bed and Sliding Body. Figure 2 shows the soil filling process. The slope was filled by layers of loess taken from the southern suburbs of Xi'an City. The weight of the compacted soil was 18.3 kN/m^3, and the moisture content was 15%. After layered filling, the sliding bed and sliding body were compressed to a target density. After the filling of slopes, the slope surface was made according to the designed shape, and the excess soil was removed. In order to reduce the boundary effect, three through grooves were designed in the sliding body and filled with sand.

2.3.2. Sliding Surface. Figure 3 depicts the photo of sliding surface. After filling the sliding bed soil, the sliding surface was made according to the shape of the designed sliding surface and double-layer plastic films were put on the sliding surface to simulate the sliding zone. On the basis of the no-pile test, we determined the load and the landslide thrust when the sliding body was in the ultimate equilibrium state using the reverse calculation: $c = 3.5$ kPa, and $\varphi = 16^\circ$.

2.3.3. Model Pile and Connecting Beam. Figures 4 and 5 show the precast reinforcement concrete and connecting beam of micropiles, respectively. To facilitate the burial of test instruments, the model piles used in this test were reinforced concrete prefabricated piles, and the micropiles were poured with fine aggregate concrete. The concrete strength grade was C25, and the cement strength grade was 42.5 R. The length of the pile was 4 m, the diameter of the pile was 60 mm, and the reinforcement method was 4 φ 6.5. The top of the piles was linked with the angle steel to simulate the connecting beam.

2.4. Layout of Micropiles. Figure 6 illustrates the layout of micropiles and pressure gauges. Five rows of micropiles were laid out with 0.5 m row spacing and 0.8 m row middle pile spacing.

2.5. Measurements

2.5.1. Pressure Measurements for the Micropiles. The pressure gauges were embedded along the piles in front of and behind piles to monitor the distribution and variation of landslide thrust of the micropiles, resistance from the sliding body behind the piles, and resistance from the sliding bed. Figure 7 depicts the position and number of pressure gauges.

2.5.2. Strain Measurements of the Micropiles. To test the bending moment of the micropile, strain gauges were pasted in pairs before and after the longitudinal bar of the tested piles. The spacing of the strain gauges is 10 cm. After measuring the strains of different parts of the micropile, the bending moments can be obtained by

$$M = \frac{\mathrm{EI}\left(\varepsilon_+ + \varepsilon_-\right)}{h}. \tag{1}$$

In the formula, M is the bending moment, N·m; EI is the flexural rigidity of the micropile, N·m^2; ε_+, ε_- are, respectively, the tensile and compressive strains of each measuring point; and h is the distance of the tensile and compressive strain gauges at the same section, m.

2.5.3. Displacement Measurements. The displacement gauges were placed on the top of the piles as well as at the toe of the landslide model, aiming to measure the displacement of the pile group and slope deformation.

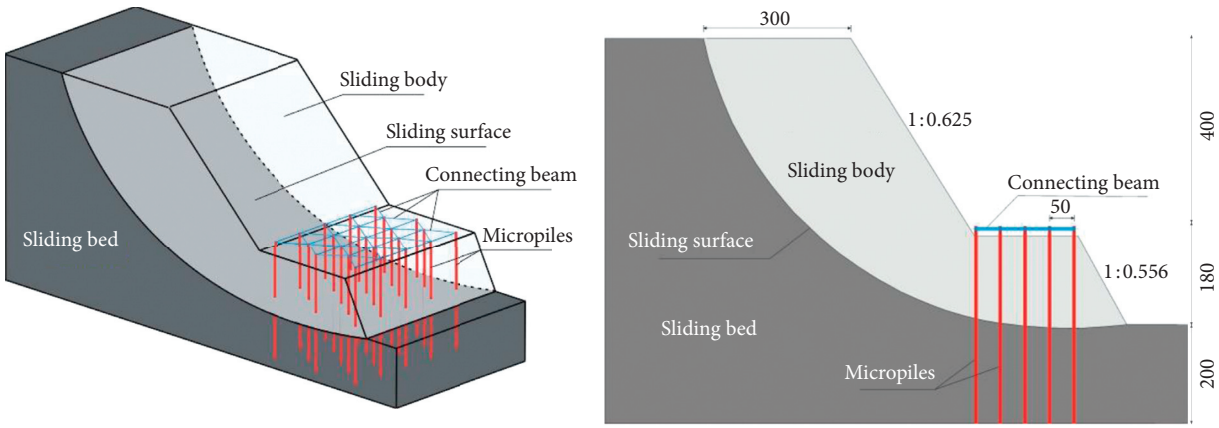

(a) (b)

Figure 1: Schematic diagram of the test model. (a) Schematic diagram of the test model; (b) sectional view of the model (unit: cm).

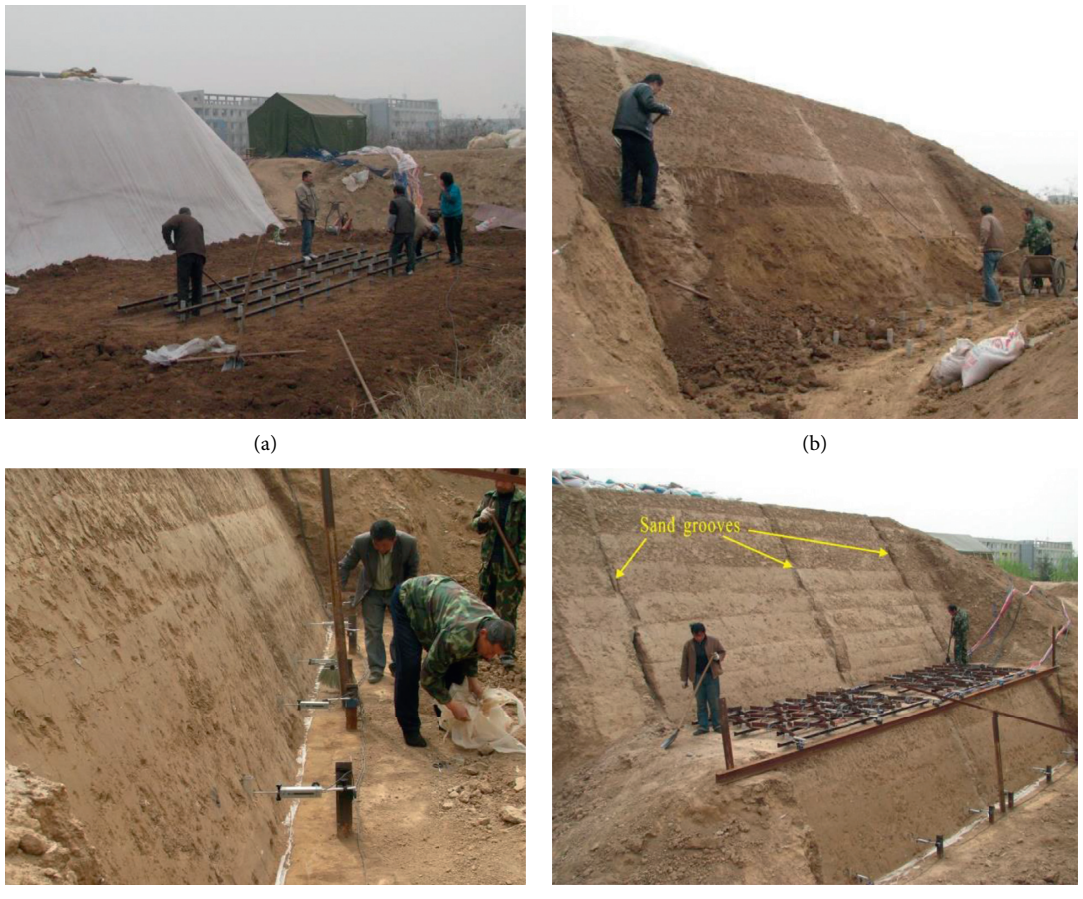

(a) (b)

(c) (d)

Figure 2: The manufacturing process of the sliding body. (a) Layered filling of soil; (b) removing excess soil; (c) excavating the landslide toe; (d) the completed test model.

2.6. Loading Condition. After model test was assembled and monitoring sensor was implemented, layers of sandbags used as the multi-stage loading were placed on the top of the landslide model. The photo of multi-stage loading is shown in Figure 8. Each loading increment was 8 kPa. At each loading step, the recording of sensors was monitored [18, 19]. After reaching the stable value, the next step of load would be applied. A total of 48 kPa loads were applied in this test, as shown in Figure 8.

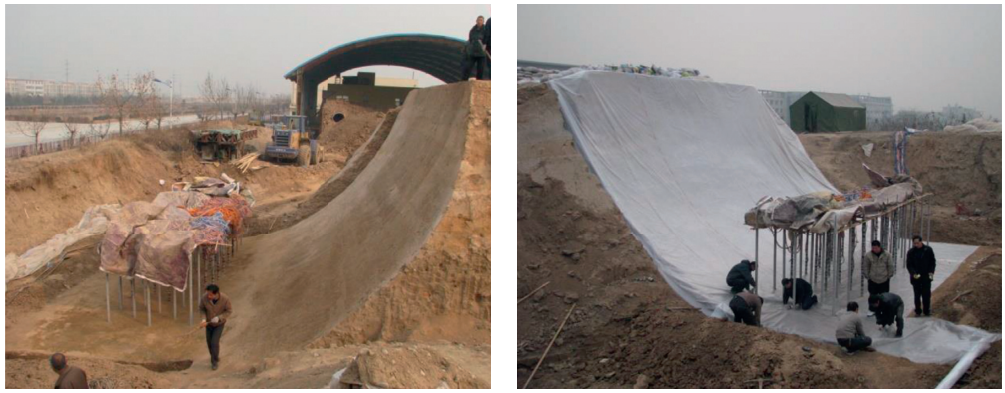

(a) (b)

Figure 3: Schematic diagram of sliding surface. (a) The sliding surface; (b) double-layer plastic films were put on the sliding surface.

(a) (b)

Figure 4: The precast reinforcement concrete micropiles: (a) Reinforcement; (b) micropiles.

Figure 5: The connecting beam on the top of micropiles.

3. Results and Analysis

3.1. Failure Modes of Micropiles. After the test, sectional excavation was conducted to observe the failure characteristic of micropile as shown in Figure 9. From the excavation section, it can be observed that the landslide completely slipped along the presupposed sliding surface and no new fracture surface occurred. The damage zone of the micropiles in each row was almost the same. The damage zone of the pile was 12 cm under the sliding surface to 15 cm over the sliding surface. Within the range of the damage, the pile body was bent with several slanted cracks. Outside the range of the damage, the pile body was almost integrated. The load-bearing segment leaned slightly toward the front

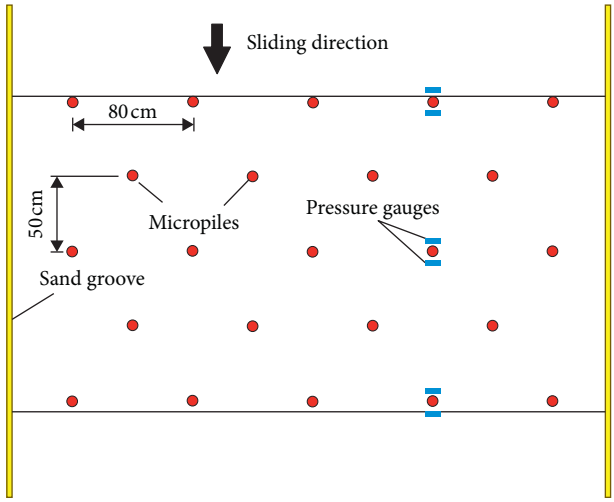

Figure 6: Layout of micropiles and pressure gauges (unit: cm).

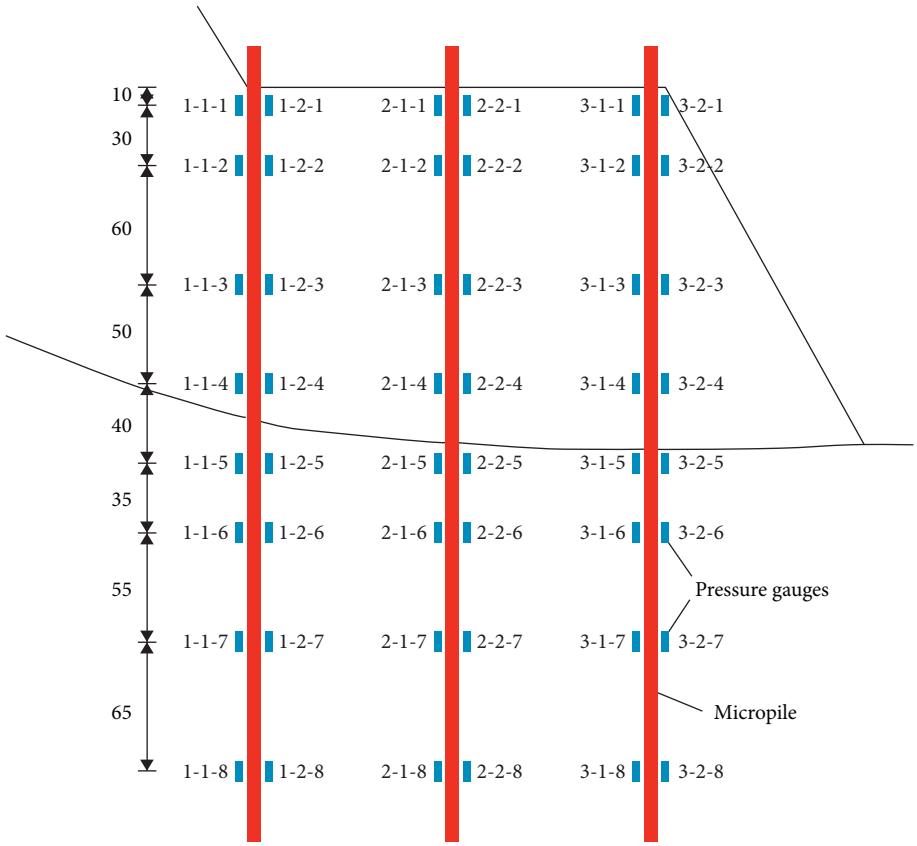

Figure 7: Distribution of the pressure gauges in vertical direction along the pile (unit: cm).

edge of the slide. Because of the deformation of the soil, there was a certain range of void area between the pile body around the sliding surface and surrounding soil. The void area around the sliding surface was located on the surface between the slide bed soil of the pile body and the slide bed soil behind the pile. By analyzing the damage conditions of the micropile, it was evident that the failure mode was composed of the bent and shear around the sliding surface.

3.2. Force Condition of Micropiles. Figure 10 shows the force distribution of the soil at each measurement point near the micropile.

Figure 11 shows the force distribution of the soil at each measurement point of the micropile. The pile section above the slipping surface was regarded as the anti-sliding segment of the pile. The pile section under the slipping surface was regarded as the anchoring section of the pile.

Figure 8: Multi-stage loading on the top of the landslide model.

(a) (b) (c) (d)

Figure 9: The damage of micropiles. (a) Overall damage of micropile groups; (b) breakage of the pile in first row near the slipping surface; (c) breakage of the pile in middle row near the slipping surface; (d) breakage of the pile in last row near the slipping surface.

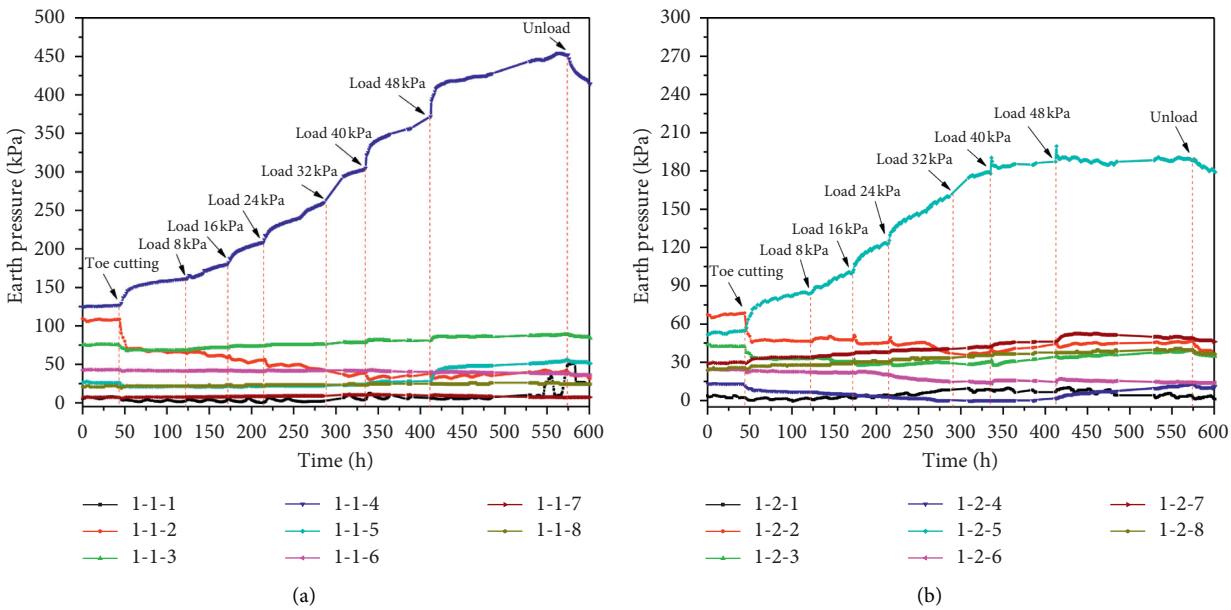

(a) (b)

Figure 10: Continued.

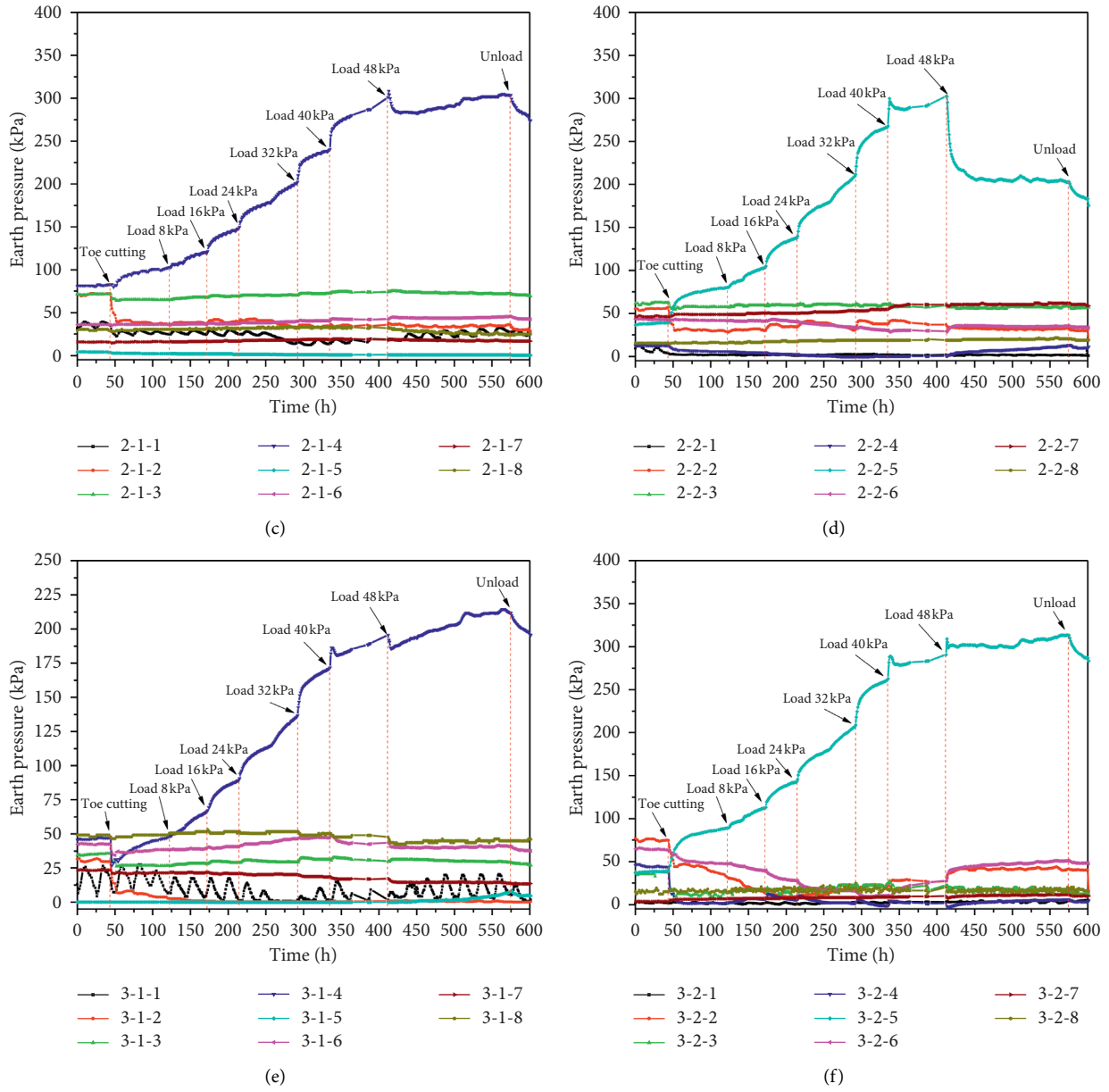

Figure 10: Earth pressure of micropiles. (a) Curves of earth pressure at measuring points before the pile in first row; (b) curves of earth pressure at measuring points behind the pile in first row; (c) curves of earth pressure at measuring points before the pile in middle row; (d) curves of earth pressure at measuring points behind the pile in middle row; (e) curves of earth pressure at measuring points before the pile in last row; (f) curves of earth pressure at measuring points behind the pile in last row.

3.2.1. Distribution of the Landslide-Thrust Force of the Pile in the First Row. Distribution of the landslide-thrust force of the pile in the first row is shown in Figures 11(a) and 12(a), including measuring points 1-1-1, 1-1-2, 1-1-3, and 1-1-4. After the filling stage, the landslide-thrust force was basically distributed in a polygonal line, which could be calculated according to trapezoid distribution in design phase. After the toe of the slope was excavated, the Earth pressure at 0.2 m over the sliding surface (1-1-4) enlarged and the Earth pressure of the other three points decreased, implying that the micropile was displaced at this time. The distribution mode of landslide thrust began to change and the point of resultant force moved close to the sliding surface. After loading, at 0.2 m over the sliding surface (1-1-4), the Earth pressure enlarged continuously. While the Earth pressure at 0.7 m over the sliding surface (1-1-3) increased slightly, meanwhile the Earth pressure at 1.3 m over the sliding surface (1-1-2) decreased slowly. Finally, the landslide thrust was distributed approximately in a triangle shape and the Earth pressure near the sliding surface was relatively large.

3.2.2. Resistance from the Sliding Body behind the Pile in the First Row. Resistance from the sliding body behind the pile in the first row is shown in Figures 11(b) and 12(a), including measuring points 1-2-1, 1-2-2, 1-2-3, and 1-2-4.

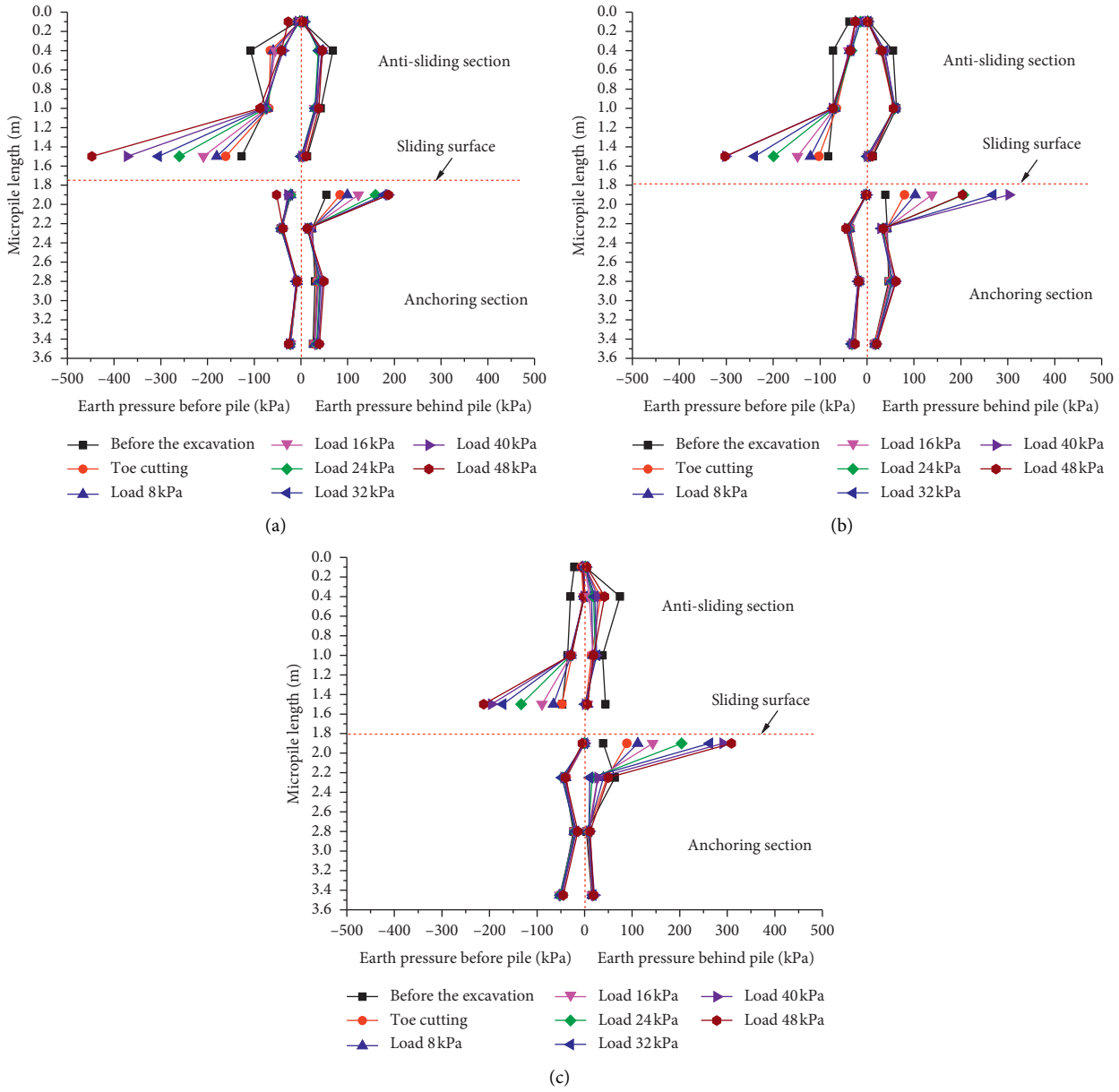

Figure 11: Distribution of the earth pressure on the micropiles. (a) Distribution of the earth pressure on the pile in first row; (b) distribution of the earth pressure on the pile in middle row; (c) distribution of the earth pressure on the pile in last row.

After excavating the toe of the slope, the Earth pressure of all four measurement points decreased. After loading, the Earth pressure at 0.2 m, 0.7 m, and 1.3 m over the sliding surface (1-2-4, 1-2-3, 1-2-2) kept decreasing, while loading to 40 kPa, the Earth pressure at the three points gradually grew larger. The Earth pressure at 1.6 m over the sliding surface (1-2-1) gradually enlarged in the loading process, and there were obvious fluctuations. Because this measurement point was close to the Earth surface, the fluctuation may have been related to the changing temperature. The anterior sliding mass resistance was basically distributed as a parabola.

3.2.3. Resistance from the Sliding Bed in front of the Pile in the First Row. Resistance from the sliding bed in front of the pile in the first row is shown in Figures 11(a) and 12(a), including measuring points 1-1-5, 1-1-6, 1-1-7, and 1-1-8. Compared with the landslide-thrust force, the Earth pressure of each measurement point in front of the pile in the anchoring section was relatively small, and this pressure remained unchanged during the loading process. Sliding bed resistance in front of the pile was distributed in a polygonal line, which could be calculated according to rectangular distribution in design phase.

3.2.4. Resistance from the Sliding Bed behind the Pile in the First Row. Resistance from the sliding bed behind the pile in the first row is shown in Figures 11(b) and 12(a), including measuring points 1-2-5, 1-2-6, 1-2-7, and 1-2-8. Before completion of model filling and excavation of the slope foot, Earth pressures at each measurement point under the sliding

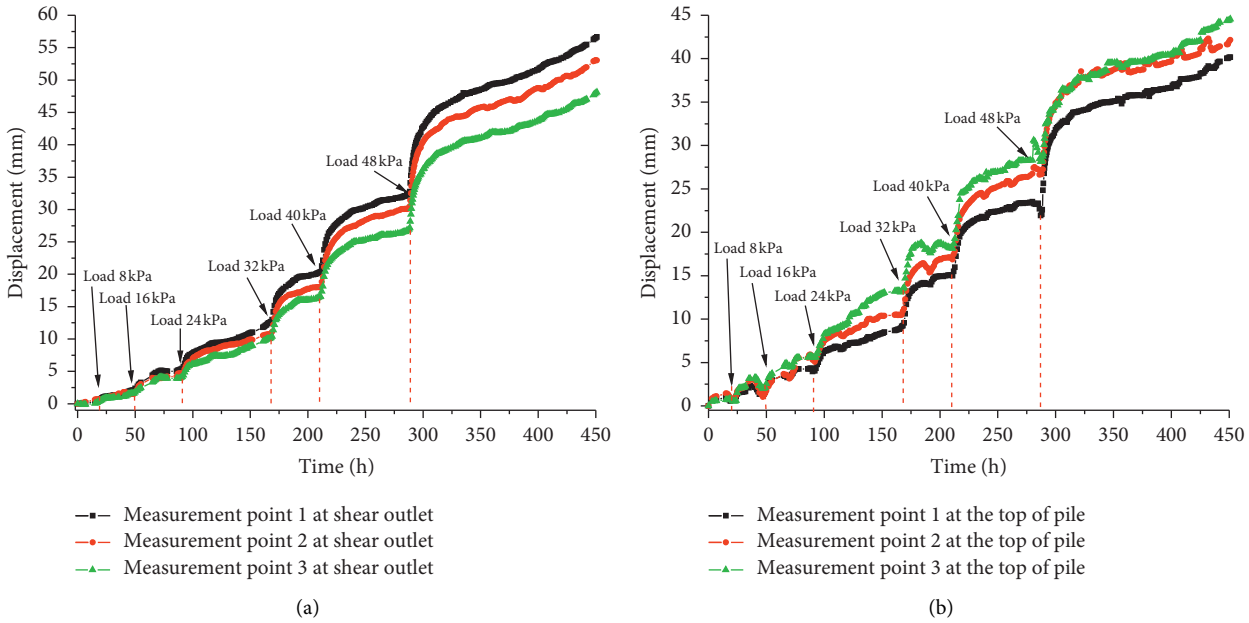

Figure 12: Displacement variation at the monitoring points. (a) Displacement curve at the toe of landslide; (b) displacement curve at the top of pile.

surface were basically equal, and resistance of the sliding bed behind the pile was distributed in a rectangular shape. Earth pressure at 0.2 m below the sliding surface (1-2-5) increased after the slope foot was excavated, and the Earth pressure at the remaining three measurement points under the sliding surface basically remained unchanged, indicating that the pile body in a certain range under the sliding surface deflected and squeezed the posterior soil body of the sliding bed. After the loading was applied, the Earth pressure at 0.2 m below the sliding surface continued to increase until the loading reached 40 kPa and then it began to be stable basically. The Earth pressure at other three measurement points was small relatively. The resistance from the sliding bed behind the pile was concentrated mainly near the sliding surface.

As shown in Figures 11 and 12, the piles in the middle row and last row behaved in a similar way to that of the pile in the first row. This distribution can be summarized as follows:

(1) The landslide thrust of the micropiles was in an approximate trapezoid distribution, and the Earth pressure near the sliding surface was larger.

(2) The landslide thrust of the first row of piles along the sliding direction was large, and the landslide thrusts of the remaining rows reduced successively.

(3) The distribution of the resistance from sliding body behind the pile was basically parabolically distributed. The Earth pressure near the sliding surface and the pile top was small and the Earth pressure in the middle part of the landslide was large.

(4) The resistance from the anterior sliding bed of the micropiles was small and changed little during the loading process. It was in a polygonal line distribution and could be calculated as rectangular distribution in design.

(5) In the early stage, the resistance from the posterior sliding bed was in a polygonal line or rectangular distribution. After loading, the Earth pressure near the sliding surface varied greatly, whereas the Earth pressure at the other measurement points varied slightly and resistance from anterior sliding bed was distributed mainly near the sliding surface.

(6) The force variations of micropiles demonstrated good timeliness. Force was applied to the three rows of micropiles at the same time, and displacement and damage occurred simultaneously.

3.3. Variation of Displacement at Measurement Points. Figure 12 shows the displacement evolution during loading. The displacement at the top of pile and the shear outlet of landslide increased slowly in the early stage of loading. After the loading reached 32 kPa, the displacement of each measurement point increased rapidly. Hence, the pile entered a critical state when loading reached 32 kPa. Up to 40 kPa, the displacement at the top of micropiles was about 15 mm, corresponding to the failure stage.

Comparing Earth pressure variation and displacement evaluation, the results were consistent, showing the pile was damaged after 40 kPa loading.

3.4. Bending Moment of Pile Body. Based on strain gauge data, the bending moment distribution of each row of piles was obtained as shown in Figure 13.

Although the bending moments of each row of piles were slightly different, the variation mode along the pile was the

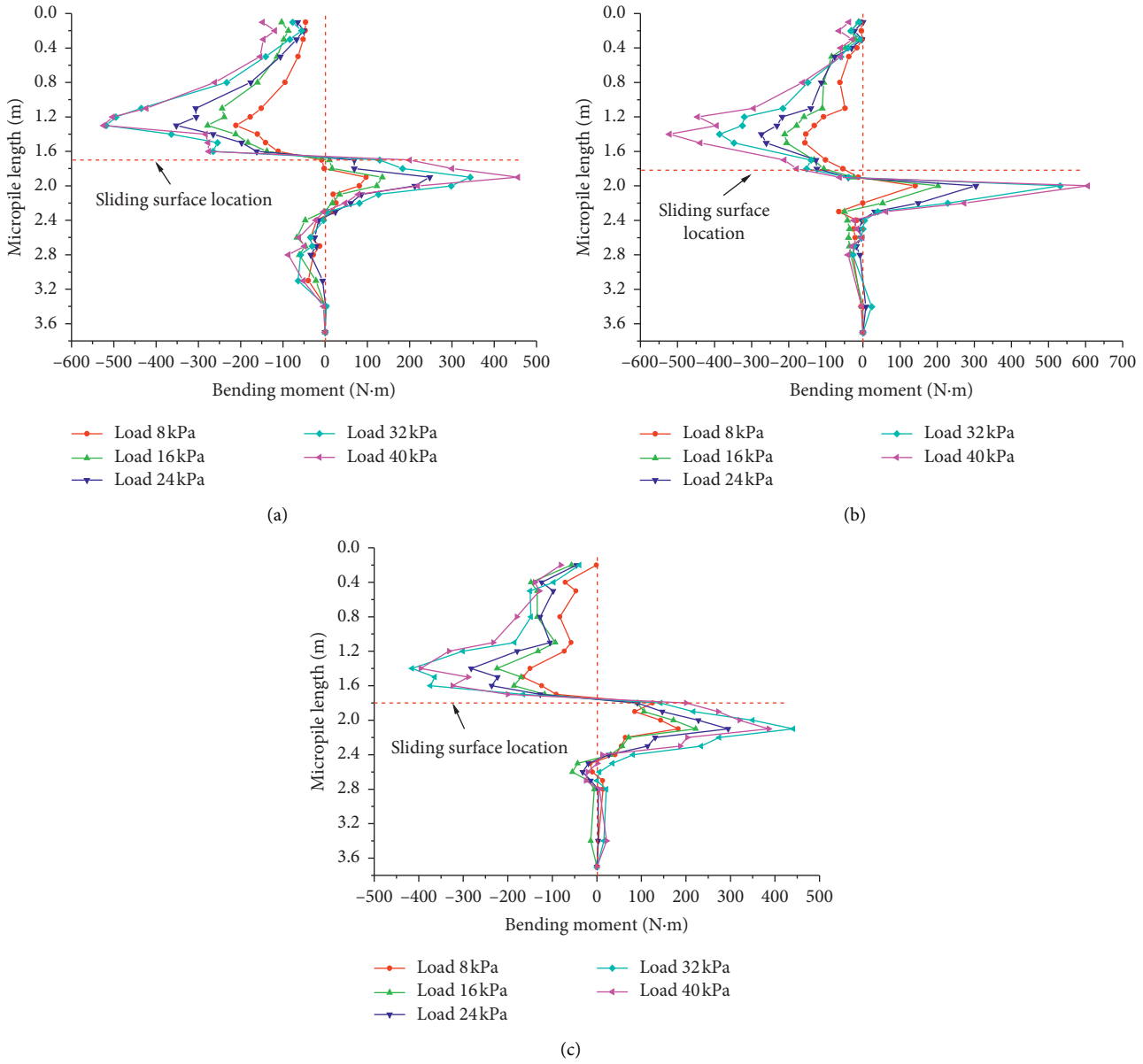

Figure 13: Bending moment of micropiles. (a) Bending moment of the pile in first row; (b) bending moment of the pile in middle row; (c) bending moment of the pile in last row.

same. The load-bearing sections of the pile body were all subjected to negative bending moments (positive tension on the sliding side and negative tension on the back side) and were distributed mainly within the pile length range of half of the load-bearing section on the sliding surface. The maximum negative bending moment was at 0.4 m above the sliding surface (about seven times the diameter of the pile). The pile body of the embedded section located in the range of 0.6 m below the sliding surface was subjected to a positive bending moment. The maximum positive bending moment occurred at 0.3 m below the sliding surface (five times the diameter of the pile). The pile body from 0.6 m below the sliding surface to the bottom of the pile was subjected to a negative bending moment, with a small magnitude. After loading, the bending moments of the load-bearing section and the embedded section increased simultaneously, indicating that the load-bearing section and the embedded section of the micropiles deformed simultaneously.

4. Conclusion

A large-scale model test was performed to simulate the interaction between the micropile group and landslide. The loading-induced deformation characteristics of the micropile group under the action of a landslide were investigated. The results provide a reference for the design of a micropile group preventing the landslide. The main conclusions can be drawn as follows:

(1) When the landslide occurred, the micropiles at different rows were subjected to loads

simultaneously. Consequently, the displacement and the damage occurred simultaneously. The force distribution of micropiles of each row was basically the same.

(2) The landslide thrust of micropiles was generally in a triangle distribution, with a larger Earth pressure near the sliding surface. The resistance from the sliding body behind the pile was parabolically distributed. The larger resistance was observed from the sliding bed behind the pile to the area near the sliding surface.

(3) The load-bearing sections were all subjected to negative bending moments. The maximum negative bending moment occurred at a place seven times the diameter of the pile above the sliding surface. The pile body of the embedded section in the range of 0.6 m (10 times the diameter of the pile) below the sliding surface was subjected to a positive bending moment, with a maximum value at five times the diameter of the pile below the sliding surface.

(4) The damage condition of each row of micropiles was basically the same. The damage area was within the range of three times the diameter of pile above and below the sliding surface each. The failure mode was a combination of effect of bending and shearing near the sliding surface.

Data Availability

The data used to support the findings of this study are included within the article.

Conflicts of Interest

The authors declare no conflicts of interest.

Authors' Contributions

Xueling Liu and Jinkai Yan analyzed, wrote, and dealt with data; Jinkai Yan and Lei Liu conducted the model test; Bing Han modified the formats. All authors have read and agreed to the published version of the manuscript.

Acknowledgments

The authors thank the funding agencies that supported this research. This work was supported by China Geological Survey Project (Grant nos. 1212010814016 and DD20190287) and the Fundamental Research Funds for the Chinese Academy of Geological Science (no. JKY201909).

References

[1] F. Lizzi, *Reticulated Root Piles to Correct Landslides*, ASCE Convention, Chicago, IL, USA, 1978.

[2] R. Cantoni, T. Collotta, and V. Ghionna, "A design method for reticulated micropiles structure in sliding slopes," *Ground Engineering*, vol. 22, no. 4, pp. 41–47, 1989.

[3] S. L. Pearlman, B. D. Campbell, and J. L. Withiam, "Slope stabilization using in-situ earth reinforcement," in *Proceedings of a Special Conference on Stability and Performance of Slopes and Embankment*, Berkeley, CA, USA, July 1992.

[4] I. Juran, A. Benslimane, and D. A. Bruce, "Slope stabilization by micropile reinforcement," *Landslides*, vol. 5, pp. 1718–1726, 1996.

[5] J. E. Loehr, J. J. Bowders, and J. W. Owen, "Slope stabilization with recycled plastic pins," *Transportation Research Record: Journal of the Transportation Research Board*, vol. 1714, no. 1, pp. 1–8.

[6] B. LiewSommers, R. Mario, and A. Nadir, "Design and construction of a micropile wall to stabilize a railway embankment," in *Proceedings of the Deep Foundations Institute Annual Conference on Deep Foundations: Emerging Technologies*, Vancouver, British Columbia, Canada, October 2004.

[7] L. L. Zeng, X. Bian, L. Zhao, Y. J. Wang, and Z. S. Hong, "Effect of phosphogypsum on physiochemical and mechanical behaviour of cement stabilized dredged soil from Fuzhou, China," *Geomechanics for Energy and the Environment*, vol. 25, Article ID 100195, 2021.

[8] X. Bian, L. L. Zeng, X. Z. Li, X. S. Shi, S. M. Zhou, and F. Q. Li, "Fabric changes induced by super-absorbent polymer on cement and lime stabilized excavated clayey soil," *Journal of Rock Mechanics and Geotechnical Engineering*.

[9] X. Bian, J. K. Yan, and W. Zhang, "Observed performance of highway embankment over soft marine clay: a case study in Wenzhou, China," *Advances in Civil Engineering*, vol. 2020, Article ID 8813832, 2020.

[10] Y. B. Zhou, X. H. He, and M. Ma, "Study on the application of micro-group piles in highway cutting," *Journal of Anhui Jianzhu University*, vol. 26, no. 4, pp. 45–52, 2018.

[11] L.-L. Zeng, Z.-S. Hong, and Y.-J. Cui, "On the volumetric strain-time curve patterns of dredged clays during primary consolidation," *Géotechnique*, vol. 65, no. 12, pp. 1023–1028, 2015.

[12] J. R. Richards, D. Thomas, and J. Rothbauer Mark, "Lateral loads on pin piles (micropiles)," in *Proceedings of Sessions of the Geosupport Conference: Innovation and Cooperation in Geo*, Reston, VA, USA, January 2004.

[13] K. Konagai, Y. Yin, and Y. Murono, "Single beam analogy for describing soil-pile group interaction," *Soil Dynamics and Earthquake Engineering*, vol. 23, no. 3, pp. 31–39, 2003.

[14] Z. Y. Liang, J. Y. Rao, Z. Q. Chen et al., "Study on ultimate flexural bearing capacity of mini pile featuring steel tube and centered steel bar," *Railway Engineering*, vol. 58, no. 11, pp. 99–102, 2018.

[15] H. Chen, Y. F. Zhang, X. M. Zhang et al., "Full-scale model experiments on anti-sliding characteristics of high-pressure grouting steel-tube micropiles," *Rock and Soil Mechanics*, vol. 41, no. 2, pp. 428–436, 2020.

[16] Y. F. Zhang, S. W. Wei, W. J. Zhou et al., "Model test study on anti-sliding behaviours of multiple segmented grouting steel pile group structure," *Chinese Journal of Rock Mechanics and Engineering*, vol. 38, no. 5, pp. 982–992, 2019.

[17] S. Y. Hu, Q. Cai, and C. J. Li, "A study of the physical model test of debris landslide reinforcement with three row micropiles," *Hydrogeology & Engineering Geology*, vol. 45, no. 3, pp. 56–62, 2018.

[18] X. Bian, Y.-J. Cui, L.-L. Zeng, and X.-Z. Li, "State of compacted bentonite inside a fractured granite cylinder after infiltration," *Applied Clay Science*, vol. 186, p. 105438, 2020.

[19] X. Bian, Y.-J. Cui, and X.-Z. Li, "Voids effect on the swelling behaviour of compacted bentonite," *Géotechnique*, vol. 69, no. 7, pp. 593–605, 2019.